Fabrication of Polymer Optical Waveguides by Digital Ultraviolet Lithography

Zuoqin Ding, Han Wang, Taige Li, Xia Ouyang, Yaocheng Shi, and A. Ping Zhang, *Senior Member, IEEE*

***Abstract*—We present the design, fabrication and characterization of polymer optical waveguides using a digital ultraviolet (UV) lithography. Grayscale optical exposure with a nonlinear compensation in quadratic form is applied to minimize the stitching loss of the transition zone between two adjacent subpatterns. Proximity effects in lithography process are compensated based on an exposure dose-map that is calculated under the approximation of scattered light pixel with a Gaussian distribution. The bending loss and propagation loss of the fabricated polymer waveguides are experimentally characterized to be around 0.1 dB/90°-bend and 0.238 dB/mm, respectively. Moreover, 1 × 2 multimode-interference power splitter, 1 × 2 Y-branch power splitter and microring resonator are demonstrated to show the feasibility of the lithography technology on rapid fabrication of waveguides. Such a UV lithography technology flexibly manipulates huge-number light pixels for all-digital grayscale and dynamic optical exposure and thus can enable the fabrication of novel optical waveguide-based devices and sensors, such as 2.5D waveguides for multimode crossing and polymer waveguide devices for biosensing.**

***Index Terms*—Digital lithography, polymer optical waveguides, proximity effects, integrated optics.**

I. Introduction

With the advantages of low cost, easy fabrication and high transmission, polymer-based optical waveguides have been extensively studied and applied in various fields, such as photonic integrated devices and optical label-free biosensors [1]-[8]. In the applications of integrated devices, polymer waveguides show excellent flexibility in vertical direction, which renders great promise in vertical effective refractive index (RI) modulation and 2.5D or 3D structure development, such as Maxwell fisheye-based multimode crossings [3]-[6]. In addition, due to their good compatibility with different substrates and materials, polymer waveguides are attractive for hybrid integration of photonic devices or chips with different functional materials [7]-[9]. In the applications of label-free biosensors, polymer waveguides can directly absorb proteins on its surface and immobilize them by covalent bond, thus the bimolecular information can be easily detected by combining them with optical waveguide structures [9], [10]. Various fabrication technologies have been utilized to fabricate polymer waveguides, including the optical lithography [11], [12], laser direct writing [13], E-beam lithography [14]. Traditional optical lithography provides an efficient way for rapid fabrication of polymer waveguides. However, it lacks of flexibility in the fabrication of gray-scale features for e.g. vertical integration. Laser direct writing or e-beam lithography technologies have good flexibility but are commonly less efficient because of their inherent single-spot scanning nature. These bottleneck problems may be overcome by using digital ultraviolet lithography (DUL).

The DUL uses high-speed spatial light modulator, such as digital micro-mirror device (DMD), with millions of pixels as virtual dynamic mask, which renders great promise in the all-digital high-throughput fabrication of polymer waveguide with complicated geometry [15-17]. DMD consists of millions of micro-mirrors that can be tilted to represent “ON” and “OFF” states. In the “ON” state, light is reflected by micro-mirrors and forms an optical pattern of great many pixels on the substrate after passing through an optical projection system. In the “OFF” state, light is directed elsewhere and the corresponding pixels appear dark. The state of each micro-mirror can be rapidly controlled by computer with the image data of designed model. Such a digital light processing nature render its ability for grayscale exposure and 3D microfabrication [15], [16].

To fabricate polymer waveguides under single-mode operation, the resolution of DUL system should be below 2 μm. To achieve the goal, many efforts have been made to improve the resolution of the DMD-based lithography technology. For example, D. H. Lee demonstrated a design of projection lens to reduce the single-pixel size of micro-mirrors from 13.68 μm to 4 μm [18]. T. L. Laidig and H. J. Jeong used an anti-blazed DMD to enhance the resolution, in which a 180-degree phase shift was introduced between adjacent micro-mirrors [19]. K. Kim *et al.* presented a wobulation technique to improve the resolution, where pixels overlap by half a pixel and the edges of diagonal patterns are smoothly created with additional

Manuscript received xxx; revised xxx; accepted xxx. Date of publication xxx. This work was partially financially supported by PolyU General Research Fund under Grant No.: G-YBY2 and Hong Kong RGC GRF under Grant PolyU 152211/19E. (*Z. Ding and H. Wang have contributed equally to the work. Corresponding author: A. Ping Zhang.*)

Z. Ding, H. Wang, T. Li, X. Ouyang and A. P. Zhang are with the Photonics Research Centre, Department of Electrical Engineering, The Hong Kong Polytechnic University, Kowloon, Hong Kong SAR, China (e-mail: azhang@polyu.edu.hk).

Z. Ding and Y. Shi are with the Center for Optical and Electromagnetic Research, College of Optical Science and Engineering; International Research Center for Advanced Photonics, Zhejiang University, Hangzhou, China (e-mail: yaocheng@zju.edu.cn).

subpatterns [20].

In this paper, we present the fabrication of high-quality polymer optical waveguides using a high-resolution DUL based on high-magnification reduction projection optics and small-pixel-size DMD, whose pixel size is 7.6 μm. In particular, proximity effects are corrected by an exposure dose-map calculated with the approximation of Gaussian-like light pixel. Stitching loss is depressed by creation of nonlinear transition zone in quadratic form. In the experiments, multiple SU-8 optical waveguides, such as multimode interference (MMI) splitter, Y-branch power splitter and micro-ring resonators (MRR) are fabricated and characterized to demonstrate the performance of the high-resolution DUL.

II. Design And Simulation

The schematic of the SU-8 waveguide considered in this paper is shown in Fig. 1(a). Ridge waveguide structure with air cladding and 4-μm thick SiO_2 insulator upon silicon wafer is used to achieve a high refractive index contrast for strong confinement of light propagating in waveguide with small bending radius. The finite difference eigenmode (FDE) solver (MODE Solutions, Lumerical Solutions Inc.) was used to design and analyze the waveguide structure. The size of the SU-8 waveguide is 2.0 μm (H) × 2.4 μm (W) so as to make it operating under single-mode condition with relatively low polarization dependence. Fig. 1(b) shows the simulated mode profiles, which indicates that only fundamental transverse electric (TE_0) and transverse magnetic (TM_0) modes are supported.

Several kinds of SU-8 waveguides, including MMI coupler, Y-branch power splitter and MRR, are designed. The working principle of MMI power splitters is based on the self-image theory [21]. For a 1 × N MMI splitter, the length L_{MMI} of the core section is typically chosen as [21]:

$$L_{MMI} = 3L_{\pi} / 4N = 3\pi / 4N(\beta_0 - \beta_1), \quad (1)$$

where L_{π} is the beat length of the two lowest-order modes, N is the number of output waveguides, β_0 and β_1 are the propagation constants of the first and second order modes, respectively. The separation W_{sp} between two output waveguides is [21]:

$$W_{sp} = (W + (\frac{\lambda}{\pi})(\frac{1}{n_r})^{2\sigma}(n_r^2 - 1^2)^{-1/2}) / N, \quad (2)$$

where W is the width of the MMI core, λ is wavelength, n_r is the refractive index of the waveguide, $\sigma = 0$ for TE mode and $\sigma = 1$ for TM mode. In our design, the width of the MMI core is chosen to be 40 μm to excite enough modes as well as to provide enough separation between two output waveguides. The eigenmode expansion propagation solver (EME solver, Lumerical Solutions Inc.) is utilized to optimize the MMI coupler. The other parameters of the MMI coupler include: the length of MMI is 774.2 μm, the separation between two output waveguides is 20.1 μm.

The 1 × 2 Y-branch power splitter consists of an input waveguide, two S-bends and two output waveguides. The radius of the S-bends is chosen to be 300 μm to attain small bending loss as well as to guarantee enough separation between the two output waveguides.

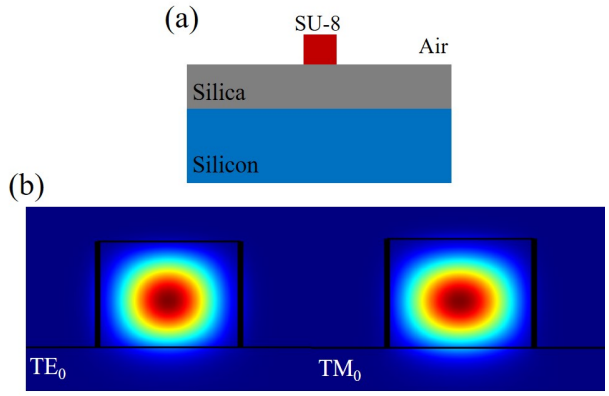

Fig. 1. (a) Schematic of the cross-section of SU-8 waveguide. (b) Simulated electrical field distributions of TE_0 and TM_0 modes of the designed waveguides.

For the design of MRR, an MMI-like gapless coupling section is introduced to achieve shorter coupling length and larger fabrication tolerance [22], [23]. Taking bending loss into consideration, the radius of the MRR is chosen to be 150 μm.

III. Fabrication And Optimization

A. Experimental Setup and Fabrication Processes

A home-developed digital UV exposure system was used in the fabrication of designed waveguides. As shown in Fig. 2, the lithography system is composed of a nano-precision motorized stage (ANT130-XY, Aerotech Inc.), a projection optics, a high-power UV light-emitting diode (L10561-215, Hamamatsu Photonics) and a high-speed DMD (DLP6500, Digital Light Innovations) [15], [24-26]. The projection optics includes two pieces of lenses purchased from Thorlabs Inc., which reduces the pitch of light pixels to ~300 nm. A digital camera is integrated to precisely local the vertical position. The designed patterns of waveguides were converted into 8-bit grayscale bitmaps and uploaded to DMD, which acts as a virtual mask for use in optical exposure process. With the assumption that a gray value g can be approximately represented by the depth of light penetration in SU-8 in the fabrication, the total exposure time t can be determined in line accordance with the Beer Lambert law [27] as:

$$t = t_0 \exp(g / c_r), \quad (3)$$

where t_0 is the threshold of exposure time, the constant c_r depends on the contents of SU-8 photoresist, such as photoinitiator and inhibitor, as well as the light intensity.

In the experiments, the silicon wafer capped with a 4-μm thick SiO_2 layer was used as the substrate. Before spin coating of SU-8, an adhesion promoter Omnicoat (Kayaku Advanced Materials, Inc.) was spun on the wafer at the speed of 3000 rpm for 30 s to promote the adhesion between SU-8 and silica. Then SU-8 2005 (Kayaku Advanced Materials, Inc.) was spin-coated at the speed of 4000 rpm for 1 min. The thickness of the SU-8 layer was measured to be ~2.1 μm. After soft baking at 65 °C

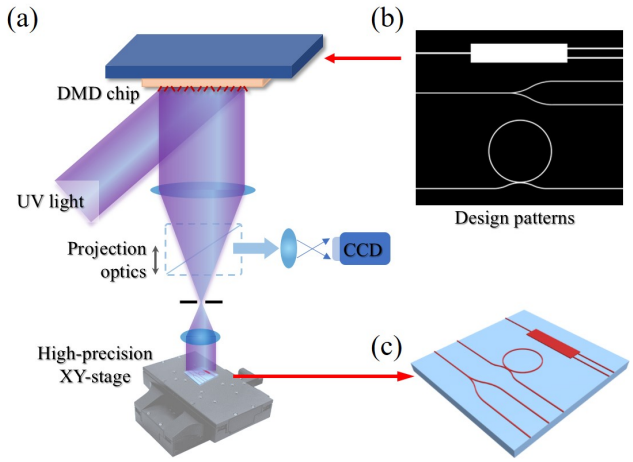

Fig. 2. (a) Schematic of the DUL system. (b) Grayscale bitmap of designed patterns acting as digital mask. (c) Schematic of end-cut waveguide structures.

for 5 min and 95 °C for 10 min, optical exposure was conducted under the light intensity of 61.91 mW/cm^2 to inscribe the designed patterns into the SU-8. Then the samples were post-baked at 65 °C for 15 min and 95 °C for 30 min. After development in 1-Methoxy-2-propyl acetate (J&K Scientific Ltd.) for 2 min, the samples were finally hard-baked at 120 °C for 1 hour. A relatively low ramping rate, i.e. about 7.1 °C/min, has been applied to the heating up and cooling down processes in both post-bake and hard-bake. After the fabrication of waveguides, the chip was cut on both sides for edge coupling. Two lensed fibers were used to couple light into and out of the waveguides. A broadband light source (from 1520 nm to 1610 nm) and an optical spectrum analyzer (OSA, Yokogawa AQ6370D) were used to measure the transmission spectra of the fabricated waveguides.

B. Proximity Effect Compensation and Seamless Stitching

It is known that the proximity effect in optical exposure will result in distortion of geometry and thereby lead to performance deterioration of the fabricated waveguides. To compensate proximity effect, we model the scattered light intensity distribution of each pixel by using a Gaussian-like distribution function:

$$P(r)=P_0\, e^{-2.773 r^2/w^2}, \qquad (4)$$

where P is the scattered light intensity of adjacent pixels with the distance of r to the central position of the light pixel with the peak intensity of P_0, w is the full width at half maximum (FWHM) of the scattered light distribution. If assume that each light pixel has the same scattered distribution, one can obtain the distribution of light intensity of all pixels of a pattern by superposing the light intensity of all adjacent pixels. With such a distribution, one can thus offset the intensity of the pixels whose intensity was increased due to the scattering of adjacent light pixels to compensate the proximity effect.

Figure 3(a) shows an example of line pattern after compensation of proximity effect. One can see that the pixels at the edge of the waveguides have higher grayscale value while the pixels in the middle of the waveguides have lower grayscale value because of heavier scattering of light. To optimize not only the exposure time but also the threshold of exposure time t_0 and the FWHM w in Eq. (4), a line pattern with half-maximum gray edge, as shown in Fig. 3(c), and an angled line pattern have been designed for use in exposure tests.

Figure 3(b) and (d) show the scanning electron microscopy (SEM) images of the fabricated line patterns when the exposure time, the threshold time t_0 and the FWHM w are 18 s, 1.8 s, and 3.0, respectively. It can be seen that both of the all-white 8-pixel wide line pattern and 9-pixel wide line pattern with half-maximum gray edge can fabricate the line waveguides with the width of 2.4 μm after optimization of these parameters. Fig. 3(e) shows the effects of different FWHM w on the fabricated patterns. One can see that some residue caused by proximity effect was observed in the inner corner when the FWHM w is 0. While a better geometry without obvious residue in the inner corner was achieved when the FWHM w is increased to 3.0, which means that the proximity effect has been well compensated. Notably, if the fabrication conditions, such as the chemical constituents, the thickness of photoresist and the intensity of exposure UV light, are changed, these parameters including the total exposure time t and the threshold of exposure time t_0 in Eq. (3) and the FWHM w in Eq. (4) need optimized again so as to fabricate best structures with depressed proximity effect.

Although a DMD chip has millions of pixels, typically 1920 × 1080 pixels, the size of its optical image projected on the substrate is about 572 × 322 μm^2 because of the use of

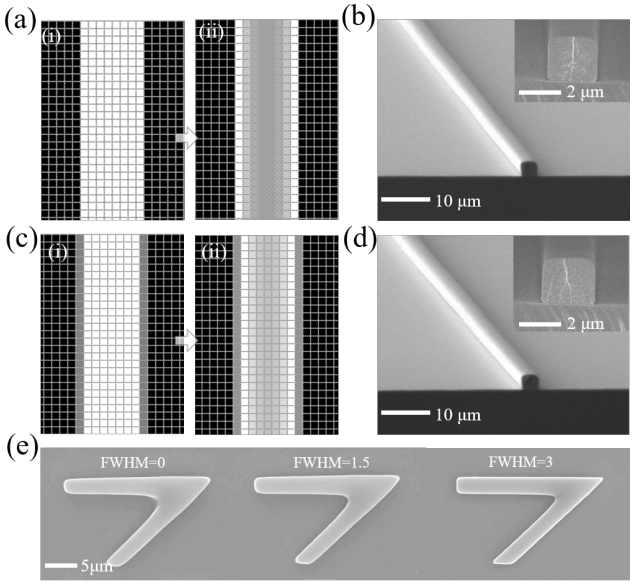

Fig. 3. (a) An 8-pixel wide line pattern before (i) and after (ii) corrected with Gaussian-like light pixel distribution. (b) SEM images of the fabricated pattern of 2.4-μm wide line waveguide. (c) A 9-pixel wide line pattern with half-maximum gray edge before (i) and after (ii) corrected with Gaussian-like light pixel distribution. (d) SEM images of the fabricated pattern of 2.4-μm wide line waveguide. (e) SEM images of the fabricated patterns of angled lines using different FWHMs.

reduction projection optics. Therefore, it is an improve process to stitch many subpatterns in the fabrication of a practical waveguide device with input/output components. To reduce optical loss of stitching misalignment, transition zones were introduced between adjacent subpatterns. We set the grayscale values, which are corresponding to the exposure doses, of the pixels in transition zone in quadratic form so as to compensate the potential width difference induced by two separated exposures. Specifically, for a transition zone defined by pixel position from x_0 to x_1, the gray values of the transition zone in two successive subpatterns are:

$$\begin{cases} g_f(x_l) = g_0(x_l)[1 - x_l + 4c(x_l - x_l^2)], \\ g_b(x_l) = g_0(x_l)[x_l + 4c(x_l - x_l^2)], \end{cases} \quad (5)$$

where g_f and g_b are the modified grayscale values of the transition zone in the current and the adjacent subpatterns, respectively, g_0 is the original grayscale value of the designed pattern, the local pixel position $x_l = (x - x_0)/(x_1 - x_0)$, c is compensation coefficient.

Figure 4(a) and (b) show the grayscale images of the transition zone with the compensation coefficients of 0.1 and -0.1, respectively. When the compensation coefficient is positive, the grayscale value of the pixels around the abutting center line is a little brighter which means the compensation of larger exposure dose (i.e. longer exposure time). When the compensation coefficient is negative, the grayscale value of the pixels around the abutting center line become smaller which indicates a decrease of exposure dose (i.e. shorter exposure time). Here, the max grayscale value of the image has been normalized to 255 so as to create 8-bit bitmaps for grayscale exposure process. Fig. 4(c) shows the measured transmission spectra of the fabricated waveguides with the compensation coefficients of -0.15, -0.1, -0.05, 0, and 0.05, and the SEM images of their corresponding stitched transition zone are shown in Fig. 4(d)-(h), respectively. The experimental results show that when the compensation coefficient is negative, the waveguide at the stitching region becomes thinner and the waveguide loss increases. When the compensation coefficient equals to or is larger than 0.05, the waveguide at the stitching region becomes a bit wider and the waveguide loss also increases. When the compensation coefficient is between -0.05 and 0, there is no observable stitching trace and the loss of the fabricated waveguide is relatively small. Notably, these optimal fabrication parameters depend on the configuration of the DUL system, such as the types of UV source and DMD and projection optics, as well as the chemical constituents and thickness of SU-8 layer. The optimization procedure described above need to be repeated to obtain new optimal parameters in case that the configuration of the system or SU-8 layer is altered.

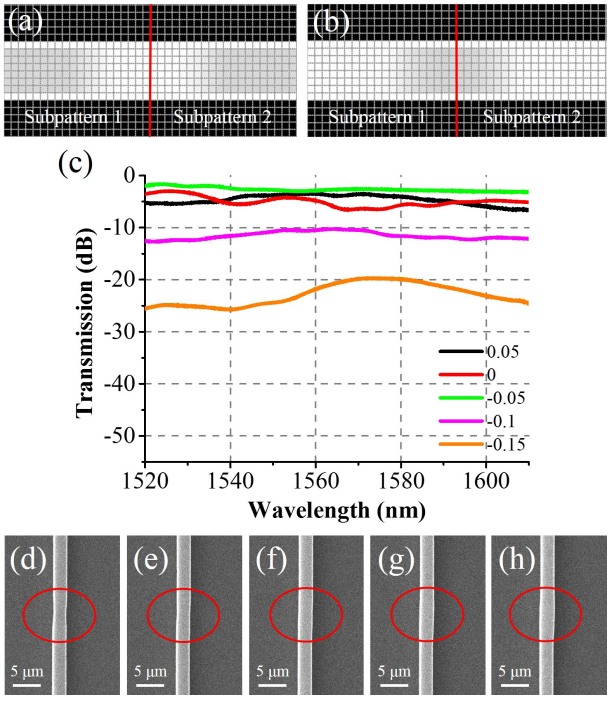

Fig. 4. Grayscale distribution maps of the stitching transition zones of two patterns when their compensation coefficients are positive (a) and negative (b), respectively. (c) Transmission spectra of the fabricated waveguides with different compensation coefficients. (d-h) SEM images of the stitching transition zone of the fabricated waveguides with different compensation coefficients of -0.15, -0.1, -0.05, 0, and 0.05, respectively.

IV. Characterization And Demonstration

A. Characterization of Bending and Propagation Losses

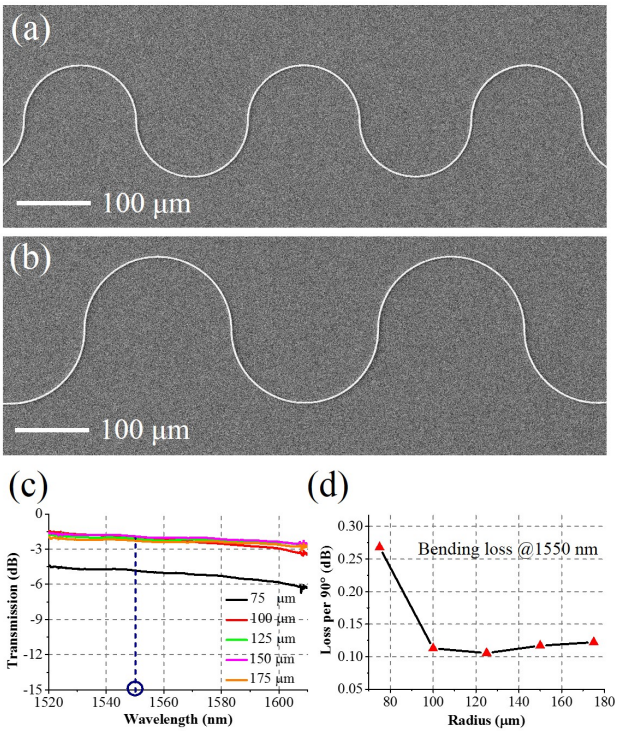

Fig. 5. (a) and (b) SEM images of the fabricated waveguides with different bending radii. (c) Measured transmission spectra of the fabricated waveguides with different bending radii. (d) Dependence of the loss on bending radius at the wavelength of 1550 nm.

In order to determine an appropriate radius for bend waveguides such as MRRs, S-bends with different radii were fabricated and characterized. The height and width of the waveguides are kept to 2.1 μm and 2.4 μm, respectively. Each waveguide includes eighteen 90°-arc waveguide sections with the fixed bending radius. Fig. 5(a) and (b) show two examples of the fabricated bend waveguides with the radii of 75 μm and 100 μm, respectively. The measured transmission spectra of the bend waveguides with the radii of 75 μm, 100 μm, 125 μm, 150 μm, and 175 μm are given in Fig. 5(c). The transmission spectra were normalized with respect to a straight waveguide with similar length so as to exclude the effects from coupling loss and propagation loss. Fig. 5(d) presents the normalized bending loss of each 90°-arc waveguide section at 1550 nm, which indicates that very low bending loss (~0.1 dB/90°) can be achieved when the radius is larger than 100 μm, which is comparable to the result achieved by traditional photolithography [28].

Therefore, the radius of bend waveguides, such as MRR or spiral waveguides, were chosen to be 150 μm so as to minimize bending loss in the experiments. Fig. 6(a) and (b) are the SEM images of the fabricated spiral waveguides with different lengths, and Fig. 6 (c) and (d) are enlarged images at different positions. Fig. 6(e) gives the measured transmission spectra of the waveguides with the lengths of 8.1 mm, 13.1 mm, 20.8 mm, and 23.9 mm, respectively. Fig. 6(f) is the measured losses at the wavelength of 1550 nm, which was extracted from Fig. 6(e). There are little ripples in the measured transmission spectra, which could be induced by the surface reflections between the lensed optical fiber and the fabricated waveguide [31] or the reflections between the micro-particles introduced during the fabrication process. The relative position, the light reflection path between the optical fiber and the waveguide facet are a little different for different measurements, and the light reflection path between different particles are also different, therefore these small spectral peaks or ripples appear at different wavelengths. One can see that the measured loss linearly increased with the length of waveguide, from which the propagation loss can be deduced to be ~0.238 dB/mm at the wavelength of 1550 nm. The loss besides transmission loss, such as edge coupling loss, was 12.8 dB which was calculated by setting the waveguide length to 0 in the fitted linear regression line. The propagation loss of our fabricated waveguides is comparable with the SU-8 waveguides fabricated by using standard lithography processes [28-30]. The main cause of such a bit high propagation loss is the scattering loss induced by tiny particles or impurities attaching on or mixed within waveguides, since the exposure processes were not conducted in the clean room, but not the sidewall roughness. The optical resolution of our DUL system is about 298 nm. Therefore, to fabricate waveguides with the width of 2.4 μm, the designed patterns of waveguides have the width of 8 pixels, which are sufficient to produce smooth boundary by 8-bit grayscale exposure technique.

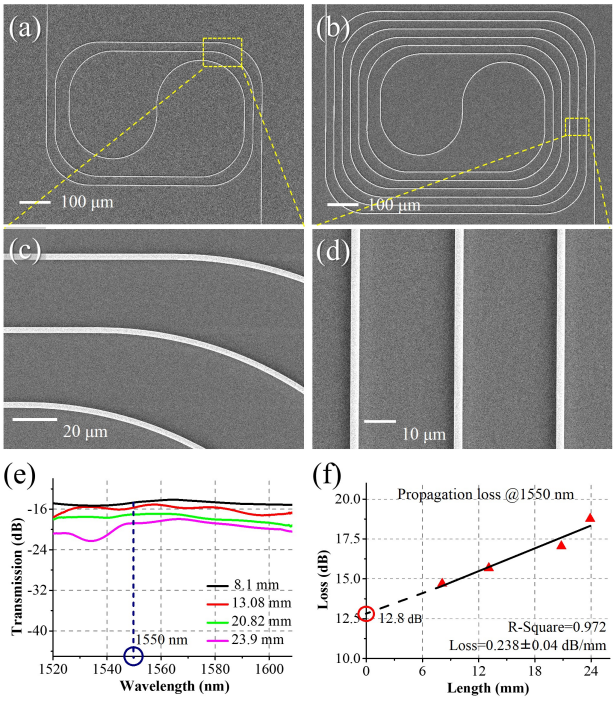

Fig. 6. (a) and (b) are the SEM images of two fabricated spiral waveguides. (c) and (d) are the enlarged images of (a) and (b) at two different positions, respectively. (e) Measured transmission spectra of the fabricated waveguides with different lengths. (f) Dependence of propagation loss on waveguide length at the wavelength of 1550 nm.

B. Demonstrations for MMI, Y-Branch Splitter and MRR

Different waveguide components were fabricated and demonstrated to verify the performance of the DUL on the fabrication of SU-8 waveguides. Two kinds of power splitters, i.e. MMI coupler and Y-branch, were fabricated and characterized. Fig. 7(a) shows the SEM image of the fabricated MMI coupler. The measured normalized transmission spectra from its two output ports are given in Fig. 7(b). It can be seen that the symmetrical MMI power splitter can split light power uniformly in a broad range of wavelength from 1520 nm to 1610 nm and the power variations of the transmission spectra are 6.5 dB and 4.0 dB, respectively. The excess loss of the fabricated MMI coupler is mainly induced by the scattering at

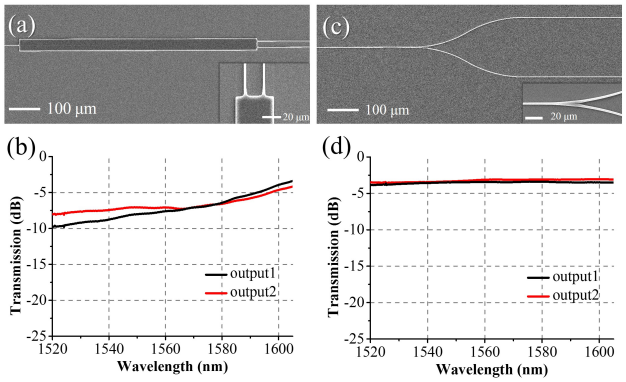

Fig. 7. (a) SEM image of the fabricated MMI power splitter. (b) Normalized transmission spectra of the fabricated MMI power splitter. (c) SEM image of the fabricated Y-branch power splitter. (d) Normalized transmission spectra of the fabricated Y-branch power splitter.

the junctions between the MMI core region and the access waveguides.

Figure 7(c) is the SEM image of a fabricated 1×2 Y-branch power splitter, which consists of one access waveguide and two branching waveguides with S-bends. The radius of the S-bends was chosen to 300 μm to minimize bending loss as well as provide enough separations between two branching waveguides. The inset in Fig. 7(c) shows the enlarged view of the Y-branch junction. Fig. 7(d) shows the measured normalized transmission spectra of the Y-branch power splitter. The spectra measured from the two output ports are close to each other and don't depend very much on the waveguide on the range of measurement. Their output power difference at 1550 nm is 0.15 dB, and it does not exceed 0.36 dB over the wavelength from 1520 nm to 1610 nm.

An MRR with a gapless coupling section was also fabricated as shown in Fig. 8(a). The radius of the ring of the MRR was chosen to be 150 μm. Fig. 8(b) is the measured transmission spectrum of the MRR at the wavelength ranging from 1520 nm to 1610 nm. Fig. 8(c) and (d) are the close-ups of the spectra at the wavelengths near 1551 nm and 1600 nm, respectively. From Fig. 8(c), it can be seen that the FSR near 1551 nm is about 1.588 nm, which is close to the simulated value of 1.575 nm. The highest quality (Q) factor corresponding to the transmission dip at the wavelength of 1600 nm is 7174, and its extinction ratio is 16.4 dB.

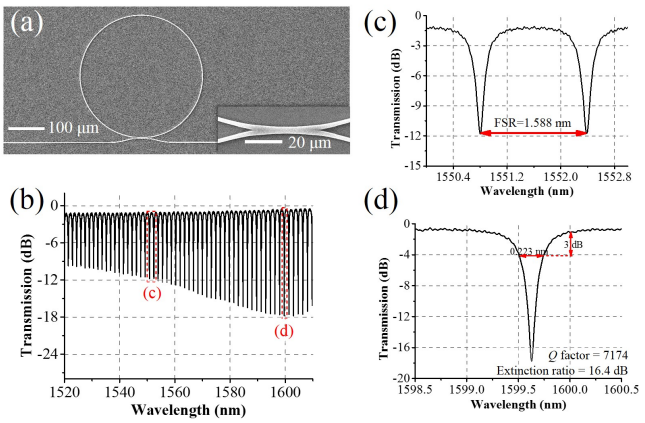

Fig. 8. (a) SEM image of a fabricated MRR. (b) Measured normalized transmission spectrum of the MRR. (c) and (d) Close-ups of transmission spectra at the wavelengths around 1551 nm and 1600 nm, respectively.

V. Conclusion

In summary, we have presented the design, fabrication, characterization of SU-8 waveguides by using a new fabrication process with a DMD-based DUL. It can not only overcome the shortage in flexibility of traditional optical lithography [28-30] but also render much higher productivity than E-beam lithography [14] and laser direct writing technologies [13]. Proximity effect induced by light scattering in SU-8 has been compensated through a numerical pre-estimation of light scattering effect so as to depress lithography resolution degradation. Moreover, strategy based on grayscale exposure method has also been demonstrated to seamlessly stitch patterns towards large-area high-quality waveguide devices.

Experiments have been demonstrated that the bending loss of the fabricated waveguide is about 0.1 dB/90°-arc when the bending radius is not smaller than 100 μm. The propagation loss is 0.238 dB/mm at the wavelength of 1550 nm. Moreover, the fabricated MMI and Y-branch power splitters can uniformly split input power at a broad range of wavelength from 1520 nm to 1610 nm. The fabricated MRR has a Q-factor over 7100 and an extinction ratio of about 16 dB.

It is believed that such a grayscale and dynamic optical exposure technology is very promising to fabricate the waveguides with 2.5D and even 3D structures, such as Maxwell fisheye-based multimode crossings. After integrating with machine vision technology, it can be further developed towards intelligent adaptive lithography technology for development of novel waveguide devices and biosensors.

Acknowledgement

We thank Hong Kong RGC GRF (Grant No.: PolyU 152211/19E) and PolyU General Research Fund (Grant No.: G-YBY2) for financial support in part.

References

[1] B. Yang, Y. Zhu, Y. Jiao, L. Yang, Z. Sheng, S. He, and D. Dai, "Compact arrayed waveguide grating devices based on small SU-8 strip waveguides," *J. Lightw. Technol.,* vol. 29, no. 13, pp. 2009-2014, Jul. 2011.

[2] L. Yang, B. Yang, Z. Sheng, J. Wang, D. Dai, and S. He, "Compact 2×2 tapered multimode interference couplers based on SU-8 polymer rectangular waveguides," *Appl. Phys. Lett.,* vol. 93, no. 20, pp. 203304, Nov. 2008.

[3] X. Wang, W. Jin, Z. Chang, and K. S. Chiang, "Buried graphene electrode heater for a polymer waveguide thermo-optic device," *Opt. Lett.,* vol. 44, no. 6, pp. 1480-1483, Jan. 2019.

[4] Q. Huang, Y. Wu, W. Jin, and K. S. Chiang, "Mode multiplexer with cascaded vertical asymmetric waveguide directional couplers," *J. Lightw. Technol.,* vol. 36, no. 14, pp. 2903-2911, Apr. 2018.

[5] Q. Huang and K. S. Chiang, "High-order-mode-pass mode (de)multiplexer with a hybrid-core vertical directional coupler," *J. Lightw. Technol.,* vol. 37, no. 16, pp. 3932-3938, Feb. 2019.

[6] S. Li et al, "Universal multimode waveguide crossing based on transformation optics," *Optica,* vol. 5, no. 12, pp. 1549-1556, Dec. 2018.

[7] X. Zhang, A. Hosseini, X. Lin, H. Subbaraman, and R. T. Chen, "Polymer-based hybrid-integrated photonic devices for silicon on-chip modulation and board-level optical interconnects," *IEEE J. Sel. Top. Quantum Electron,* vol. 19, no. 6, pp. 3401115, Dec. 2013.

[8] Y. Enami *et al.,* "Hybrid polymer/sol–gel waveguide modulators with exceptionally large electro–optic coefficient," *Nature Photon.,* vol. 1, no. 3, pp. 180-185, Jul. 2007.

[9] M. Wang *et al.,* "Highly sensitive biosensor based on UV-imprinted layered polymeric–inorganic composite waveguides," *Opt. Express,* vol. 20, no. 18, pp. 20309-20317, Aug. 2012.

[10] J. Ren *et al.,* "Organic silicone Sol–Gel polymer as a noncovalent carrier of receptor proteins for label-free optical biosensor application," *ACS Appl. Mater. Interfaces.,* vol. 5, no. 2, pp. 386-394, Dec. 2012.

[11] J. Dong, K. S. Chiang, and J. Wei, "Compact three-dimensional polymer waveguide mode multiplexer," *J. Lightw. Technol.,* vol. 33, no. 22, pp. 4580-4588, Jun. 2015.

[12] L. Jin, X. Fu, B. Yang, Y. Shi, and D. Dai, "Optical bistability in a high-Q racetrack resonator based on small SU-8 ridge waveguides," *Opt. Lett.,* vol. 38, no. 12, pp. 2134-2136, Jun. 2013.

[13] A. Landowski, D. Zepp, S. Wingerter, G. V. Freymann, and A. Widera, "Direct laser written polymer waveguides with out of plane couplers for optical chips," *Apl Photonics,* vol. 2, no. 10, pp. 106102, Mar. 2017.

[14] Y. Xin, G. Pandraud, Y. Zhang, and P. Frensh, "Single-Mode Tapered Vertical SU-8Waveguide Fabricated by E-Beam Lithography for Analyte Sensing," *Sensors,* vol. 19, no. 15, pp. 3383:1-12, Jun. 2019.

[15] M. Yao, J. Wu, A. P. Zhang, H. Y. Tam, and P. K. A. Wai, "Optically 3-D μ-printed ferrule-top polymer suspended-mirror devices," *IEEE. Sens. J.,* vol. 17, no. 22, pp. 7257-7261, Aug. 2017.
[16] X. Ouyang, K. Zhang, J. Wu, D. S. Wong, Q. Feng, L. Bian, and A. P. Zhang, "Optical μ-printing of cellular-scale microscaffold arrays for 3D cell culture," *Sci. Rep.,* vol. 7, no. 8880, pp. 8880:1-8, Aug. 2017.
[17] T. Yoon, C. S. Kim, K. Kim, and J. Choi, "Emerging applications of digital micromirror devices in biophotonic fields," *Opt. Laser Techonol.,* vol. 104, pp. 17-25, Feb. 2018.
[18] D. H. Lee, "Optical system with 4 μm resolution for maskless lithography using digital micromirror device," *J. Opt. Soc. Korea,* vol. 14, no. 3, pp. 266-276, Sep. 2010.
[19] T. L. Laidig and H. J. Jeong, "Resolution enhanced digital lithography with anti-blazed dmd," U.S. Patent *0 210 346*, Jul. 26, 2018.
[20] K. Kim, S. Han, J. Yoon, S. Kwon, H. K. Park, and W. Park, "Lithographic resolution enhancement of a maskless lithography system based on a wobulation technique for flow lithography," *Appl. Phys. Lett.,* vol. 109, no. 23, pp. 234101, Dec. 2016.
[21] L. B. Soldano and E. C. M. Pennings, "Optical multi-mode interference devices based on self-imaging: principles and applications," *J. Lightw. Technol.,* vol. 13, no. 4, pp. 615-627, Apr. 1995.
[22] P. Liu and Y. Shi, "Simultaneous measurement of refraction index and temperature using a dual polarization ring," *Appl. Optics.,* vol. 55, no. 13, pp. 3537-3541, May. 2016.
[23] Z. Ding, P. Liu, J. Chen, D. Dai, and Y. Shi, "On-chip simultaneous sensing of humidity and temperature with a dual-polarization silicon microring resonator," *Opt. Express,* vol. 27, no. 20, pp. 28649-28659, Sep. 2019.
[24] J. Wu, M. Yao, F. Xiong, A. P. Zhang, H. Y. Tam, and P. K. A. Wai, "Optical fiber-tip Fabry-Perot interferometric pressure sensor based on an in situ μ-printed air cavity," *J. Lightw. Technol.,* vol. 36, no. 17, pp. 3618-3623, Sep. 2018.
[25] J. Wu, M.-J. Yin, K. Seefeldt, A. Dani, R. Guterman, J. Yuan, A. P. Zhang, and H. Y. Tam, "In situ μ-printed optical fiber-tip CO_2 sensor using a photocrosslinkable poly(ionic liquid)," *Sens. Actuators. B*, vol. 259, pp. 833–839, Apr. 2018.
[26] M. Yao, Y. Zhang, X. Ouyang, A. P. Zhang, H.-Y. Tam, and P. K.A. Wai, "Ultracompact optical fiber acoustic sensors based on a fiber-top spirally-suspended optomechanical microresonator," *Opt. Lett.,* vol. 45, no. 13, pp. 3516-3519, May. 2020.
[27] X. Ouyang, Z. Yin, J. Wu, C. Zhou, and A. P. Zhang, "Rapid optical μ-printing of polymer top-lensed microlens array," *Opt. Express,* vol. 27, no. 13, pp. 18376-18382, Jun. 2019.
[28] B. Yang, L. Yang, R. Hu, Z. Sheng, D. Dai, Q. Liu, and S. He, "Fabrication and characterization of small optical ridge waveguides based on SU-8 polymer," *J. Lightw. Technol.,* vol. 27, no. 18, pp. 4091-4096, Sep. 2009.
[29] S. Madden, Z. Jin, D. Choi, S. Debbarma, D. Bulla, and B. Luther-Davies, "Low loss coupling to sub-micron thick rib and nanowire waveguides by vertical tapering," *Opt. Express,* vol. 21, no. 3, pp. 3582-3594, Feb. 2013.
[30] Y. Jiao, Y. Zhu, X. Hong, Y. Shi, L. Xu, and S. He, "An integrated optical mixer based on SU8 polymer for PDM-QPSK demodulation," *IEEE Photon. Technol. Lett.,* vol. 23, no. 20, pp. 1490-1492, Oct. 2011.
[31] X. Wang, X. Quan, M. Liu, and X. Cheng, "Silicon-nitride-assisted edge coupler interfacing with high numerical aperture fiber," *IEEE Photon. Technol. Lett.,* vol. 31, no. 5, pp. 349-352, Mar. 2019.

Zuoqin Ding received the B.Eng. degree in optics engineering from Nanjing University of Posts and Telecommunications, Nanjing, China, in 2017. Currently, she is a Ph.D. student of Zhejiang University, Hangzhou, China.

Her research interests mainly focus on optical waveguide based sensing technology.

Han Wang received the B.Eng. and M.Sc. degrees from Shenzhen University and City University of Hong Kong in 2018 and 2020, respectively. Currently, she is a Ph.D. student of The Hong Kong Polytechnic University, Hong Kong, China.

Her research interests mainly focus on optical waveguide sensors and optofluidic biochips.

Taige Li received the B.Eng. degree in electronic engineering from City University of Hong Kong, Hong Kong, China, in 2020. Currently, he is an M.Phil. student of The Hong Kong Polytechnic University, Hong Kong, China.

His research interests mainly focus on optical microring resonator sensors and biochips.

Xia Ouyang received the B.Eng. and Ph. D degrees in optics engineering from Huazhong University of Science and Technology, and Hong Kong Polytechnic University in 2015 and 2020, respectively.

His research interests mainly focus on micro/nano-fabrication technologies and optical biosensors.

Yaocheng Shi received the B.Eng. degree from the Department of Optical Engineering, Zhejiang University, Hangzhou, China, in 2003 and the Ph.D. degree from the Royal Institute of Technology (KTH), Stockholm, Sweden, in 2008. Then he joined in Zhejiang University as an assistant professor and became a professor in 2016. He has authored more than 100 refereed international journal papers.

His research activities are in the design and fabrication of photonic integrated devices.

A. Ping Zhang (SM'17) received the B.Sc. and M.Sc. degrees from Zhejiang University (ZJU), Hangzhou, China, in 1997 and 2000, respectively, and the Ph.D. degree from The Hong Kong Polytechnic University (PolyU), Hong Kong, China, in 2003.

Since 2003, he was with the Department of Optical Engineering, ZJU and served as a Lecturer and an Associate Professor until 2012. He was a Research Scholar with the Institute for Lasers, Photonics, and Biophotonics, State University of New-York at Buffalo during the period of 2006–2008, and with the Department of NanoEngineering, University of California, San Diego, in 2011, respectively. He joined the Department of Electrical Engineering, PolyU, as an Associate Professor in 2012 and now is the Professor at the same department. His research interests include optical micro-/nano-fabrication technologies, photonic devices, sensors, and microsystem.

Prof. Zhang is a Senior Member of the Optical Society of America (OSA) and Institute of Electrical and Electronics Engineers (IEEE).